Two-Dimensional Negative Thermal Expansion in a Crystal of LiBO₂

Xingyu Zhang, Xingxing Jiang,* Maxim S. Molokeev, Naizheng Wang, Youquan Liu, and Zheshuai Lin*

Read Online

ACCESS | Metrics & More | Article Recommendations | SI Supporting Information

ABSTRACT: Negative thermal expansion (NTE), violating the common sense of "thermal expansion and cold contraction" effects, is a novel temperature-responding behavior of great scientific and technical significance. Herein, we report a two-dimensional (2D) NTE behavior in a crystal of $LiBO_2$, which is constructed by graphite-like $[LiBO_2]_\infty$ layers. This intriguing thermal property originates from the synergistic effect of the distortion of in-plane $[LiO_3]$ bases in $[LiO_4]$ tetrahedra and the rotation of $[BO_3]$ triangles in the $[LiBO_2]_\infty$ layer, driven by the force perpendicular to the layer owing to the large interlayer separation as temperature increases. Remarkably, the in-plane and out-of-plane Li−O bonds within the $[LiO_4]$ tetrahedra have nearly the same bond strength and exhibit the similar variation with respect to temperature, and this is quite different from the common sense on the 2D NTE behavior in layered structures that the intralayer atomic interaction must be much stronger than the interlayer ones. Our study deepens the understanding of the 2D NTE mechanism and would promote the exploration for NTE materials.
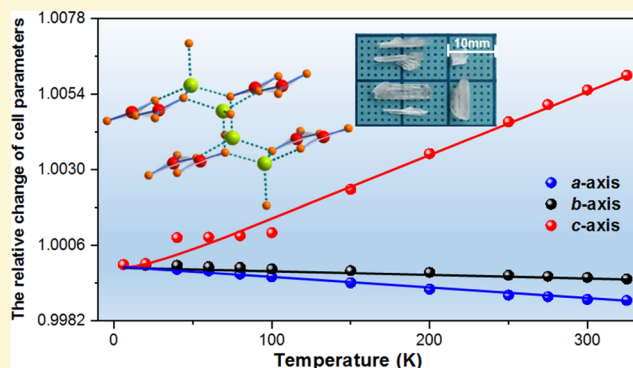
INTRODUCTION

Negative thermal expansion (NTE) materials, with the capability to contract along specific directions as temperature increases, provide a simple and effective method to buffer the "heat expansion and cold contraction" effect in conventional materials[1−3] and thus hold significant application prospects for enhancing the heat resistance of apparatus under temperature-fluctuating conditions.[4−6] Meanwhile, the counterintuitive "heat-shrinkage" response in NTE materials embraces rich mechanisms,[7−11] which is quite helpful for understanding the fundamental and novel physicochemical properties in materials. Until now, quite a few NTE material systems have been exploited, such as ZrW_2O_8,[12] $PbTiO_3$-family,[13,14] Mn_3GaN-family,[15,16] $Sc_2W_3O_{12}$-family,[17] ScF_3-series,[18,19] Prussian blue,[20,21] and $Tb(Co, Fe)_2$,[22,23] with the mechanisms including transversal vibration of bridged atoms,[24] magneto volume effects,[25] spontaneous volume ferroelectrostriction,[26] and interatomic charge transfer.[27] Even though intensive efforts in this field have been in progress for decades, the search for new NTE material systems and the investigation of structure−property relationships are still very active.[28,29]

It is known that the compounds with layered structures have large structural anisotropy and are able to manifest the two-dimensional (2D) NTE behavior.[30−32] With the increase in temperature, the 2D layers in these structures often prominently separate from each other. Driven by the perpendicular-to-layer force from the colossal interlayer separation, the microscopic units protruding from the layers, which are usually surrounded by the (quasi-) rigid units in-

plane, would be dragged toward the interlayer interstices. As the (quasi-) rigid unit experiences negligibly small expansion with respect to the temperature, the out-of-plane force would shrink the area of the layers so as to generate the 2D NTE behavior. Actually, this structure−property relationship has been summarized by the membrane effect or the Lifshitz mechanism.[31] Since the prominent interlayer separation is the prerequisite for the occurrence of 2D NTE in the layered structures, the related 2D NTE material exploration has been entirely focused on the materials with the much stronger interlayer interaction than the intralayer counterpart. Guided by such a structural prototype, several 2D NTE materials with layered structures have been discovered, such as graphite,[33] BN nanosheets,[34] $TlGaSe_2$,[35] $Ag[tcm]$,[36] $KBBF$,[37] β-CuN_3,[38] and so on. Herein, we report a 2D NTE effect in a crystal of lithium metaborate ($LiBO_2$) with layered structures. Different from other 2D NTE-layered compounds,[33−38] the interlayer and intralayer atomic interactions are in a similar strength in $LiBO_2$, suggesting that this work would provide another perspective for understanding the 2D NTE behaviors in layered compounds. The potential optical application of 2D NTE in $LiBO_2$ is also discussed.
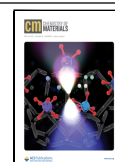
■ EXPERIMENTAL AND CALCULATION METHODS

Sample Preparation. $LiBO_2$ powder was synthesized by solid-state reaction. The ingredients Li_2CO_3 and H_3BO_3, without further purification, are ground in a stoichiometric ratio and left to set for at least 1 day at 373 K to remove H_2O. The mixture was heated gradually up to 923 K in 7 days and kept at 923 K for 1000 min with several careful intermediate grinding. After naturally cooling to room temperature, white $LiBO_2$ powder is obtained. Crystal growth was implemented in an electric vertical furnace under the control of an AI-808P digital microprocessor temperature programmer-controller. The synthesized $LiBO_2$ powder (200 g) was put into an 80 mm diameter Pt crucible and heated to 1123 K at 3 K/min. After holding for 6 h to homogenize the mixture, the melt was naturally cooled to room temperature to acquire a seed crystal. With the regrowth progress with the seed crystal in the flux following the above process, single crystals in subcentimeter size can be obtained.

Variable-Temperature Powder X-ray Diffraction. Variable-temperature powder X-ray diffraction (XRD) was performed on the as-synthesized polycrystalline sample by Bruker D8 ADVANCE (Cu-Kα radiation, 6−300 K) and Rigaku SmartLab powder diffractometers (Cu-Kα radiation, 100−850 K). The angular scanning range was set from 10 to 90° with a step size of 0.01°, and the scanning rate was set to 0.05 s/step and 15°/min for the Bruker D8 ADVANCE and Rigaku SmartLab apparatus, respectively. The lattice parameters of $LiBO_2$ were refined by the Le Bail profile[39] fitted by TOPAS 4.2,[40] and thermal expansion coefficients were fitted by PASCal software.[41]

Variable-Temperature Raman Spectra. Variable-temperature Raman spectra on the as-grown crystal were collected via LabRAM HR Evolution equipped by a solid-state laser with a wavelength of 532 nm, and the spectra were recorded from 123 to 603 K with an interval of 30 K. The wavenumber scanning range is from 100 to 1500 cm^{-1}. The peak positions were determined by the Gauss−LorenCross fitting with a chi^2 tolerance of 1×10^{-6}.

Optical Transmission Spectrum. The NIR−vis−UV transmission spectrum was measured on an Agilent Cary 5000 spectrophotometer over the spectral range of 190−3000 nm. The infrared spectrum from 3000 to 6000 nm was measured on an Excalibur 3100 Fourier transform infrared spectrometer.

First-Principles Calculation. First-principles lattice dynamics and structure simulations were performed by plane-wave pseudopotential density functional theory (DFT),[42] using CASTEP software.[43] The functionals developed by Perdew, Burke, and Ernzerhof (PBE)[44] in the form of a generalized gradient approximation (GGA)[45] is adopted to describe the exchange-correlation energy so as to search the electronic ground state. Norm-conserving pseudopotential[46] was chosen to model the effective interaction between the valence electrons and atom cores. The kinetic energy cutoff was set as 800 eV and the Monkhorst-Pack grid interval[47] was set to less than 0.04 Å^{-1}. The atomic positions at respective temperature were refined by geometry optimization with the cell parameters fixed at experimental values, in which the Broyden−Fletcher−Goldfarb−Shanno (BFGS)[48] minimization algorithm was used. The Raman spectrum and atomic vibration assignment were calculated by linear response formalism,[49] in which the phonon frequencies were obtained by the second derivative of the total energy with respect to a given perturbation. The band gaps were predicted by the hybridized PBE0 functionals.[50] The bond energy of Li−O bonds was calculated via the binding energy calculation on Li_2O with the same lengths of constituent Li−O bonds in $LiBO_2$.

■ RESULTS AND DISCUSSION

The crystal structure of $LiBO_2$ was determined by Zachariasen,[51] and it crystallizes in the monoclinic space group $P2_1/C$ with the cell parameters (at room temperature) of $a = 5.838(2)$ Å, $b = 4.348(1)$ Å, $c = 6.449(2)$ Å, and $\beta = 115.12(2)°$. The lithium and boron atoms are coordinated with four and three oxygen atoms to construct $[LiO_4]$ tetrahedra (Figure 1a) and planar $[BO_3]$ triangles (Figure
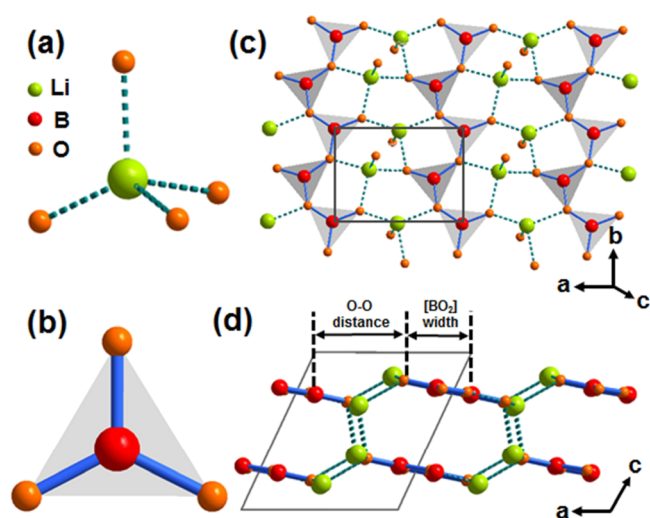
Figure 1. Crystal structure of $LiBO_2$. (a) $[LiO_4]$ tetrahedron; (b) planar $[BO_3]$ triangle; (c) $[LiBO_2]_\infty$ layer, viewed along the c-axis; and (d) crystal structure viewed along the b-axis. The black box indicates the unit cell.

1b), respectively. By sharing the oxygen corners, $[BO_3]$ triangles connect with each other to form the one-dimensional zigzag $[BO_2]_\infty$ chain along the b-axis. The $[BO_2]_\infty$ chains are connected to the (LiO_3) bases within the $[LiO_4]$ tetrahedra to form the graphite-like $[LiBO_2]_\infty$ layer in which the $[Li_2BO_3]$ and $[LiB_2O_3]$ hexatomic rings are alternatively arranged along the (a, b) plane (Figure 1c). The $[LiBO_2]_\infty$ layers are interconnected by the out-of-plane Li−O bonds (Figure 1d), whose bond length (2.0027 Å) is almost the same with the in-plane cousins varying from 1.9449 to 1.9639 Å (Table S2). Accordingly, the lattice constants of a-, b-, and c-axes are determined by the sum of the O−O distance in $[LiO_4]$ tetrahedra and the width of $[BO_2]_\infty$ chains, by the length of $[BO_2]_\infty$ chains, and by the out-of-plane Li−O bond, respectively (Figure 1c,d).

The variable-temperature powder X-ray diffraction (VT-XRD) on the as-synthesized polycrystalline sample shows that neither a new peak emerges nor an old peak vanishes from 6 to 850 K, confirming the thermodynamic stability of $LiBO_2$ (Figure S1). Regardless of the diffraction peaks from small amounts of $Li_2B_4O_7$ impurities and the copper sample hold, as displayed in Table S1, one can see that the refined errors of the cell parameters (less than 0.0005 Å) are always smaller than the variation of the cell parameters (larger than 0.001 Å), and this confirms that the refined cell parameters are accurate enough to identify the NTE property in $LiBO_2$. Since the data between 6 and 100 K and between 100 and 850 K were collected by two respective XRD apparatus, an overall shifting occurs between the two sets of refined cell parameters. Here, the cell parameters below 100 K were corrected overall by the difference between values at 100 K in the two sets of data, and their original values are listed in Table S1. The cell parameter refinement reveals that as the temperature increases from 6 to 325 K, the a- and b-axes anomalously decrease from 5.8472 (5) to 5.8405 (2) Å (by −0.11%) and from 4.3514 (3) to 4.3494 (2) Å (by −0.05%), respectively, which indicates the NTE behavior along these two axes. In comparison, the c-axis increases from 6.4185 (5) to 6.4571 (2) Å (by 0.60%), exhibiting the normal positive thermal expansion (PTE) property (Figure 2a). As $LiBO_2$ belongs to the monoclinic
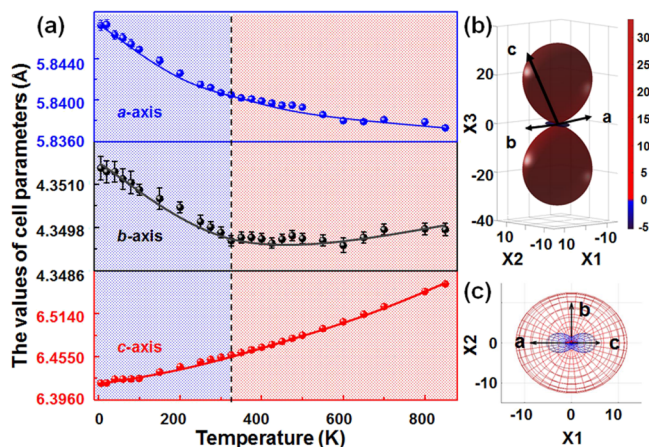
Figure 2. Thermal expansion in LiBO₂. (a) Variation of cell parameters versus temperature. To eliminate the overall shifting of the cell parameters resulting from the change of XRD apparatus, the data below 100 K were corrected by the difference (−0.0001, −0.0013, and 0.0012 Å for *a*-, *b*-, and *c*-axes, respectively) between the values at 100 K in two sets of data. (b) Three-dimensional (3D) distribution of the direction-dependent thermal expansion coefficients in which the crystallographic axes were displayed as black arrows. (c) 2D distribution of the direction-dependent thermal expansion coefficients within the (X_1, X_2) plane in which the positive and negative values are represented by red and blue grids, respectively.

$P2_1/c$ space group, the thermal principal axes do not coincide with crystallographic axes. The thermal principal axes (X_1, X_2, and X_3) and the corresponding thermal expansion coefficients were fitted by the PASCal program developed by Cliffe and Goodwin[41] (Figure 2b,c). The transformation relation between the two sets of axes is:

$$\begin{bmatrix} X_1 \\ X_2 \\ X_3 \end{bmatrix} = \begin{bmatrix} -0.9727 & 0 & 0.2322 \\ 0 & 1 & 0 \\ 0.5634 & 0 & 0.8262 \end{bmatrix} \begin{bmatrix} a \\ b \\ c \end{bmatrix}$$

The thermal expansion coefficients along the thermal principal axes X_1, X_2, and X_3 are −5.39 (12), −1.47 (3), and 33.37 (76) MK⁻¹, respectively, confirming the 2D-NTE property with an area thermal expansion coefficient of −6.86 (15) MK⁻¹ in LiBO₂. Within the 2D-NTE temperature range, the volume expansion coefficient was fitted to be a normally positive value of 26.96 (78) MK⁻¹. Above 325 K, the 2D-NTE behavior terminates and the NTE property is only maintained along the *a*-axis.
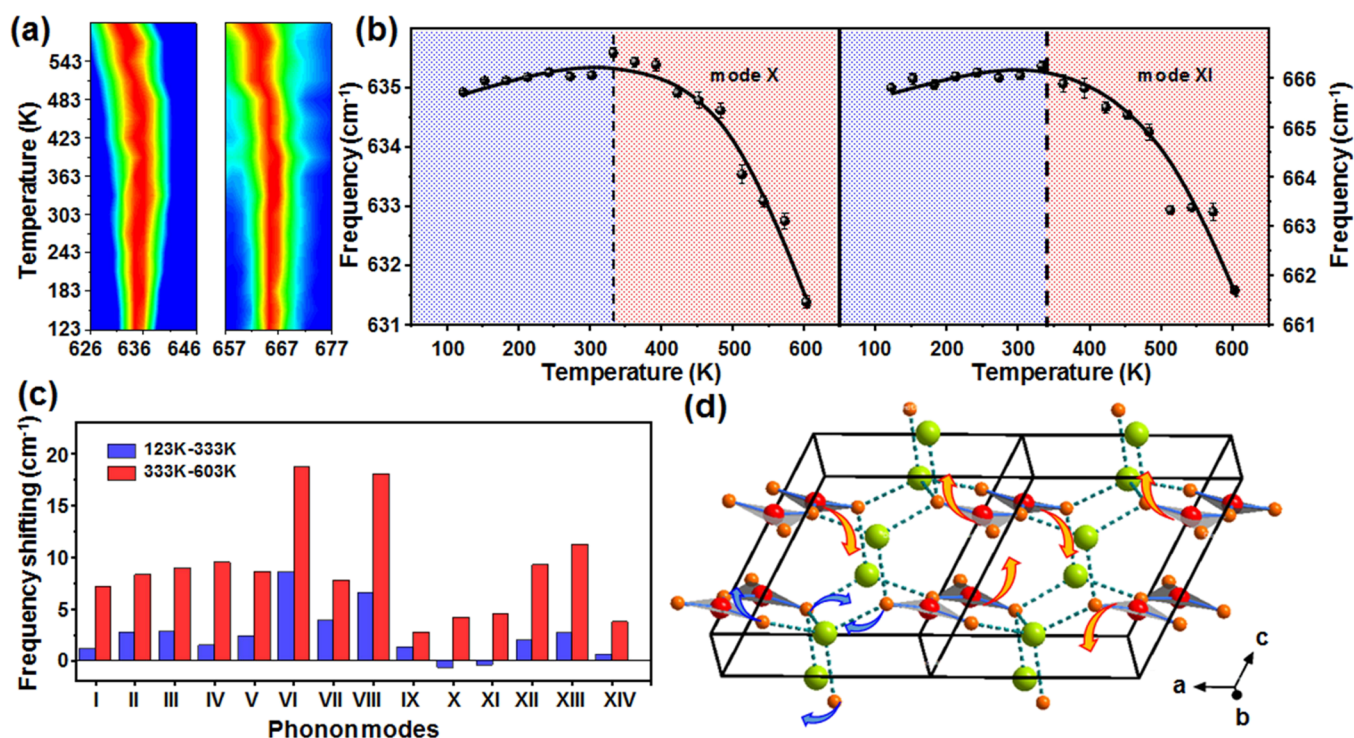
To unravel the mechanism of the 2D-NTE property in LiBO₂, the bond lengths and angles at respective temperatures were refined by high-precision first-principles simulations, since the exact atomic position variations of light lithium, boron, and oxygen atoms are difficult to be experimentally determined by XRD. It is revealed that as temperature increases from 6 to 325 K, the out-of-plane Li−O bond is elongated by 0.210% (from 2.002 to 2.007 Å in the calculated values, Figure 3a), which gives rise to the prominent PTE along the *c*-axis (Table S2). Stretched by the out-of-plane Li−O bonds, the lithium atoms are shifted toward the convex of [LiO₄] tetrahedra and the average value of the ∠O−Li−O in the (LiO₃) bases decreases from 110.887 to 110.515° (by −0.335%), which makes the (LiO₃) bases contracted (Figure 3a,c and Table S3). In comparison with the Li−O bonds, the variation of B−O bonds is negligibly weak (with an average
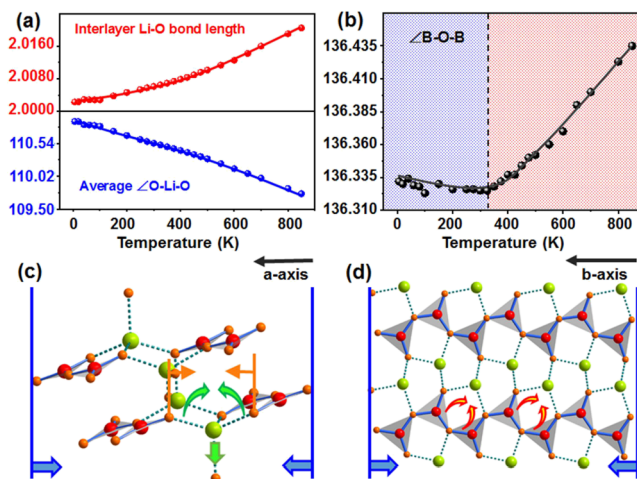
Figure 3. Temperature-induced structural modification accounting for the 2D-NTE property. (a) Variation of the interlayer Li−O bond length and the average ∠O−Li−O in the (LiO₃) base of the [LiO₄] tetrahedron. (b) ∠B−O−B versus temperature. (c) Schematic for the NTE along the *a*-axis; the stretching of out-of-plane Li−O bonds is represented by the green straight arrow, the decrease of ∠O−Li−O in the (LiO₃) base is represented by green curved arrows, and the contraction of the O−O distance is represented by orange arrows, respectively. (d) Schematic for the NTE along the *b*-axis. The rotation between [BO₃] triangles are represented by yellow curved arrows.

elongation of 0.005%, Table S2), and the main temperature-induced modification in the [BO₂]∞ chain is the rotation of the [BO₃] triangles along the *b*-axis (Figure 3b,d). With regard to the *a*-axis, the contraction effect from the decreasing ∠O−Li−O is more prominent than the expansion effect from the elongation of B−O bonds in the [BO₃] groups, and it eventually gives rise to the NTE along this direction (Figure 3c). On the other hand, the stretching of in-plane Li−O bonds causes ∠B−O−B, the angle between the neighboring [BO₃] triangles, to decrease from 136.332 to 136.325° (by −0.005%, Table S3), leading to the NTE behavior along the *b*-axis in the range 6−325 K (Figure 3d). Remarkably, the elongation of in-plane Li−O bonds (by the average values of 0.195%) is almost in the same magnitude with the out-of-plane cousins (by 0.210%) (Table S2), indicating that the interlayer and intralayer Li−O bonds have nearly the same bond strength. Moreover, bond energy is an explicit indicator of bond strength,[52,53] and the first-principles calculation revealed that the bond energy of the intralayer Li−O bond (average value of 1.2021 eV) is almost the same with the interlayer cousins (1.2022 eV) (Table S4). This demonstrates that the 2D NTE behavior can occur in the structure with similar in-plane and out-of-plane interaction.

The thermal expansion mechanism can also be investigated from the viewpoint of lattice dynamics,[54] and variable-temperature Raman spectrum measurements on the as-grown single crystal from 123 to 603 K were performed (Figure S4). In the Raman spectra, 14 main peaks are observed and defined as modes I to XIV successively. It is observed that the frequencies of modes I to IX and XII to XIV continuously decrease (i.e., softening) as temperature increases from 123 to 603 K, indicating that they positively contribute to the thermal expansion. On the contrary, the frequency of modes X and XI increase (i.e., hardening) as temperature increases from 123 to 333 K, while decreases from 333 to 603 K (Figure 4a,b). The hardening−softening reversal temperature 333 K of modes X

Figure 4. Lattice dynamics mechanism of the 2D-NTE property in LiBO$_2$. (a) Counter map of the Raman peaks in mode X and XI versus temperature. (b) Peak shift of mode X and XI versus temperature. (c) Frequency shifting of phonon modes in the temperature range of 123−333 K and 333−603 K. (d) Atomic vibration of modes X and XI. The deformation vibration of [LiO$_4$] and the rotation of [BO$_3$] triangles are represented by blue and yellow arrows, respectively.

and XI is close to the terminating temperature (325 K) of the 2D-NTE effect in LiBO$_2$, suggesting that they would play a crucial role in leading to the 2D-NTE behavior (Figure 4c). To assign the vibration assignment, the first-principles calculation was performed. As plotted in Figure S5, the calculated Raman spectrum agrees well with the experimental one, which confirms the feasibility of the first-principles atomic vibration assignment. It is revealed that both modes X and XI are mainly originated from the twisting vibration of oxygen atoms in [LiO$_4$] tetrahedra and the rotation of the [BO$_3$] triangle (Figure 4d). The decrease in ∠O−Li−O and ∠B−O−B (Figure 3a,b), which accounts for the 2D NTE, would shorten the distance between oxygen atoms within the [LiO$_4$] tetrahedra and between the neighboring [BO$_3$] triangles (Table S2) and strengthen these effective atomic interactions, which makes phonon frequency blue-shifted. As temperature increases above 325 K, the decrease of ∠B−O−B terminates, and this angle starts to increase, which suppresses the continuous reduction in ∠O−Li−O and eventually results in the decreasing-to-increasing transition of the effective O−O distances (Figure 3a,b, displayed in Tables S2 and S3). This makes the effective atomic interaction experience a transition from being strengthened to weakened, and consequently, the temperature-depending phonon mode changes at 333 K, which is close to the ∠B−O−B decreasing-to-increasing transition point of 325 K. Since the twisting of the [LiO$_4$] tetrahedra and the rotating of the neighboring [BO$_3$] triangles are mainly characterized by the variation of ∠O−Li−O and ∠B−O−B, the hardening of modes X and XI in the whole 2D NTE temperature range exactly confirms that the 2D NTE in LiBO$_2$ ascribes to the intercoupling ∠O−Li−O and ∠B−O−B decrease. Remarkably, the stretching vibration of all the four Li−O bonds within in the [LiO$_4$] tetrahedra is involved in the

modes X and XI, confirming that the stretching of both in-plane and out-of-plane Li−O bonds contribute to the 2D NTE behavior.

In comparison with the much weaker inter- than intralayer interaction in the previously reported Lifshitz-governed 2D-NTE materials (Table S6), LiBO$_2$ possesses a similar inter- and intralayer Li−O interaction. The discovery of 2D NTE in LiBO$_2$ clarifies that much weaker interlayer interaction than the intralayer ones is not a necessary condition for the occurrence of 2D NTE in layered structures. Instead, with a similar inter- and intralayer interaction, the corrugation in the layer could also be enlarged to stimulate a Lifshitz-governed 2D NTE.

Borates often have wide energy band gaps,[55] and the optical transmittance measurements on LiBO$_2$ were performed. As shown in Figure 5, LiBO$_2$ is transparent in the range between 190 and 5790 nm at room temperature, which covers a wide spectral range from ultraviolet, visible to near-infrared regions. First-principles calculation predicts that the ultraviolet absorption edge is 168 nm (band gap 7.38 eV) at 850 K, and as temperature decreases to 6 K, it is blue-shifted to 165 nm (band gap 7.52 eV). This demonstrates that the wide optical transmittance range would be maintained as temperature varies, which would be favorable to the high-precision optical application in temperature-fluctuating environments.

Summarily, 2D NTE behavior was discovered in the crystal of LiBO$_2$ with layered structures. By means of temperature-induced structural evolution and lattice dynamics analysis, it is revealed that the 2D NTE property in LiBO$_2$ is originated from the decrease of in-plane ∠O−Li−O and ∠B−O−B driven by the stretching of out-of-plane Li−O bonds as temperature increases. Remarkably, the stretching in the similar magnitude of both in-plane and out-of-plane Li−O bonds plays a crucial
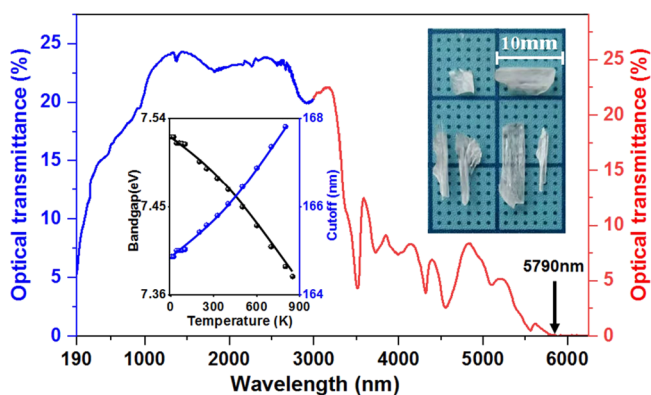
Figure 5. Optical transmission spectrum in LiBO$_2$. The morphology of the as-grown crystal and the variation of band gaps and ultraviolet cutoff versus temperature are displayed in the insets.

role in leading to the 2D-NTE behavior. This updates the common sense on 2D NTE in the layered materials that the interlayer interaction must be much weaker than the intralayer one and thus would be beneficial to the broadening of the exploration scope in NTE materials. Optical transmittance measurements show that the optical transparent range of LiBO$_2$ covers the wide spectral range from the ultraviolet, visible to near-infrared region, and the broad optical transparency would be maintained in the whole 2D-NTE temperature range. Benefiting from the NTE in combination with the excellent optical property, LiBO$_2$ holds significant application in the ultraprecise optical apparatus operated in low temperature.

ASSOCIATED CONTENT

ⓈⒾ Supporting Information

The Supporting Information is available free of charge at https://pubs.acs.org/doi/10.1021/acs.chemmater.2c00621.

> Variable-temperature XRD patterns and Raman spectra, temperature-dependent crystal structures, information about the Lifshitz-governed 2D NTE materials, and theoretical optical properties at respective temperatures (PDF)

AUTHOR INFORMATION

Corresponding Authors

Xingxing Jiang − *Functional Crystals Lab, Technical Institute of Physics and Chemistry, Chinese Academy of Sciences, Beijing 100190, China;* ⓞ orcid.org/0000-0001-6068-8773; Email: xxjiang@mail.ipc.ac.cn

Zheshuai Lin − *Functional Crystals Lab, Technical Institute of Physics and Chemistry, Chinese Academy of Sciences, Beijing 100190, China; University of the Chinese Academy of Sciences, Beijing 100049, China;* ⓞ orcid.org/0000-0002-9829-9893; Email: zslin@mail.ipc.ac.cn

Authors

Xingyu Zhang − *Functional Crystals Lab, Technical Institute of Physics and Chemistry, Chinese Academy of Sciences, Beijing 100190, China; University of the Chinese Academy of Sciences, Beijing 100049, China;* ⓞ orcid.org/0000-0003-3753-7779

Maxim S. Molokeev − *Laboratory of Crystal Physics, Kirensky Institute of Physics, Federal Research Center KSC SB RAS, Krasnoyarsk 660036, Russia; Department of Physics, Far Eastern State Transport University, Khabarovsk 680021, Russia; Department of Engineering Physics and Radioelectronic, Siberian Federal University, Krasnoyarsk 660041, Russia;* ⓞ orcid.org/0000-0002-8297-0945

Naizheng Wang − *Functional Crystals Lab, Technical Institute of Physics and Chemistry, Chinese Academy of Sciences, Beijing 100190, China; University of the Chinese Academy of Sciences, Beijing 100049, China*

Youquan Liu − *Functional Crystals Lab, Technical Institute of Physics and Chemistry, Chinese Academy of Sciences, Beijing 100190, China; University of the Chinese Academy of Sciences, Beijing 100049, China;* ⓞ orcid.org/0000-0001-7979-1463

Complete contact information is available at:
https://pubs.acs.org/10.1021/acs.chemmater.2c00621

Notes

The authors declare no competing financial interest.

REFERENCES

(1) Song, Y.; Shi, N.; Deng, S.; Xing, X.; Chen, J. Negative thermal expansion in magnetic materials. *Prog. Mater. Sci.* **2021**, *121*, No. 100835.

(2) Coates, C. S.; Goodwin, A. L. How to quantify isotropic negative thermal expansion: magnitude, range, or both? *Mater. Horizons* **2019**, *6*, 211−218.

(3) Takenaka, K.; Okamoto, Y.; Shinoda, T.; Katayama, N.; Sakai, Y. Colossal negative thermal expansion in reduced layered ruthenate. *Nat. Commun.* **2017**, *8*, 14102.

(4) Du, K.; Gao, A.; Gao, L.; Sun, S.; Lu, X.; Yu, C.; Li, S.; Zhao, H.; Bai, Y. Enhancing the structure stability of Ni-rich Li-Ni$_{0.6}$Co$_{0.2}$Mn$_{0.2}$O$_2$ cathode via encapsulating in negative thermal expansion nanocrystalline shell. *Nano Energy* **2021**, *83*, No. 105775.

(5) Zhang, Y.; McDonnell, M.; Calder, S. A.; Tucker, M. G. Mechanistic insights into the superexchange-interaction-driven negative thermal expansion in CuO. *J. Am. Chem. Soc.* **2019**, *141*, 6310−6317.

(6) Song, Y.; Sun, Q.; Yokoyama, T.; Zhu, H.; Li, Q.; Huang, R.; Ren, Y.; Huang, Q.; Xing, X.; Chen, J. Transforming thermal expansion from positive to negative: the case of cubic magnetic compounds of (Zr,Nb)Fe$_2$. *J. Phys. Chem. Lett.* **2020**, *11*, 1954−1961.

(7) Ren, Z.; Zhao, R.; Chen, X.; Li, M.; Li, X.; Tian, H.; Zhang, Z.; Han, G. Mesopores induced zero thermal expansion in single-crystal ferroelectrics. *Nat. Commun.* **2018**, *9*, 1638.

(8) Pachoud, E.; Cumby, J.; Lithgow, C. T.; Attfield, J. P. Charge order and negative thermal expansion in V$_2$OPO$_4$. *J. Am. Chem. Soc.* **2018**, *140*, 636−641.

(9) Nishikubo, T.; Sakai, Y.; Oka, K.; Watanuki, T.; Machida, A.; Mizumaki, M.; Maebayashi, K.; Imai, T.; Ogata, T.; Yokoyama, K.; Okimoto, Y.; Koshihara, S. Y.; Hojo, H.; Mizokawa, T.; Azuma, M. Enhanced negative thermal expansion induced by simultaneous charge transfer and polar-nonpolar transitions. *J. Am. Chem. Soc.* **2019**, *141*, 19397−19403.

(10) Miao, P.; Lin, X.; Koda, A.; Lee, S.; Ishikawa, Y.; Torii, S.; Yonemura, M.; Mochiku, T.; Sagayama, H.; Itoh, S.; Ikeda, K.; Otomo, T.; Wang, Y.; Kadono, R.; Kamiyama, T. Large magneto-volume effect induced by embedding ferromagnetic clusters into

antiferromagnetic matrix of cobaltite perovskite. *Adv. Mater.* **2017**, *29*, No. 1605991.

(11) Li, Q.; Lin, K.; Liu, Z.; Hu, L.; Cao, Y.; Chen, J.; Xing, X. Chemical Diversity for Tailoring Negative Thermal Expansion. *Chem. Rev.* **2022**, DOI: 10.1021/acs.chemrev.1c00756.

(12) Ma, Y.; Zhang, Q.; Zhao, K.; Liu, C.; Zhang, B.; Zhang, X.; Zhou, Y. Tunable negative thermal expansion of ultralight ZrW_2O_8/ Graphene hybrid metamaterial. *Carbon* **2019**, *153*, 32−39.

(13) Ishizaki, H.; Sakai, Y.; Nishikubo, T.; Pan, Z.; Oka, K.; Yamamoto, H.; Azuma, M. Negative thermal expansion in lead-free la-substituted $Bi_{0.5}Na_{0.5}VO_3$. *Chem. Mater.* **2020**, *32*, 4832−4837.

(14) Chen, J.; Nittala, K.; Forrester, J. S.; Jones, J. L.; Deng, J.; Yu, R.; Xing, X. The role of spontaneous polarization in the negative thermal expansion of tetragonal $PbTiO_3$-based compounds. *J. Am. Chem. Soc.* **2011**, *133*, 11114−11117.

(15) Takenaka, K.; Takagi, H. Giant negative thermal expansion in Ge-doped anti-perovskite manganese nitrides. *Appl. Phys. Lett.* **2005**, *87*, 261902.

(16) Deng, S.; Sun, Y.; Wu, H.; Huang, Q.; Yan, J.; Shi, K.; Malik, M. I.; Lu, H.; Wang, L.; Huang, R.; Li, L.; Wang, C. Invar-like Behavior of Antiperovskite $Mn_{3+x}Ni_{1−x}N$ Compounds. *Chem. Mater.* **2015**, *27*, 2495−2501.

(17) Zou, H.; Yang, X.; Chen, B.; Du, Y.; Ren, B.; Sun, X.; Qiao, X.; Zhang, Q.; Wang, F. Thermal enhancement of upconversion by negative lattice expansion in orthorhombic $Yb_2W_3O_{12}$. *Angew. Chem., Int. Ed.* **2019**, *58*, 17255−17259.

(18) Hu, L.; Chen, J.; Xu, J.; Wang, N.; Han, F.; Ren, Y.; Pan, Z.; Rong, Y.; Huang, R.; Deng, J.; Li, L.; Xing, X. Atomic linkage flexibility tuned isotropic negative, zero, and positive thermal expansion in $MZrF_6$ (M = Ca, Mn, Fe, Co, Ni, and Zn). *J. Am. Chem. Soc.* **2016**, *138*, 14530−14533.

(19) Baxter, S. J.; Hester, B. R.; Wright, B. R.; Wilkinson, A. P. Controlling the Negative Thermal Expansion and Response to Pressure in ReO_3-type Fluorides by the Deliberate Introduction of Excess Fluoride: $Mg_{1−x}Zr_{1+x}F_{6+2x}$, x = 0.15, 0.30, 0.40, and 0.50. *Chem. Mater.* **2019**, *31*, 3440−3448.

(20) Gao, Q.; Wang, J.; Sanson, A.; Sun, Q.; Liang, E.; Xing, X.; Chen, J. Discovering large isotropic negative thermal expansion in framework compound $AgB(CN)_4$ via the concept of average atomic volume. *J. Am. Chem. Soc.* **2020**, *142*, 6935−6939.

(21) Phillips, A. E.; Fortes, A. D. Crossover between Tilt Families and Zero Area Thermal Expansion in Hybrid Prussian Blue Analogues. *Angew. Chem. Int. Ed.* **2017**, *56*, 15950−15953.

(22) Song, Y.; Chen, J.; Liu, X.; Wang, C.; Zhang, J.; Liu, H.; Zhu, H.; Hu, L.; Lin, K.; Zhang, S.; Xing, X. Zero thermal expansion in magnetic and metallic $Tb(Co,Fe)_2$ Intermetallic Compounds. *J. Am. Chem. Soc.* **2018**, *140*, 602−605.

(23) Huang, R.; Liu, Y.; Fan, W.; Tan, J.; Xiao, F.; Qian, L.; Li, L. Giant negative thermal expansion in $NaZn_{13}$-type $La(Fe, Si, Co)_{13}$ compounds. *J. Am. Chem. Soc.* **2013**, *135*, 11469−11472.

(24) Chen, J.; Gao, Q.; Sanson, A.; Jiang, X.; Huang, Q.; Carnera, A.; Rodriguez, C. G.; Olivi, L.; Wang, L.; Hu, L.; Lin, K.; Ren, Y.; Lin, Z.; Wang, C.; Gu, L.; Deng, J.; Attfield, J. P.; Xing, X. Tunable thermal expansion in framework materials through redox intercalation. *Nat. Commun.* **2017**, *8*, 14441.

(25) Song, Y.; Sun, Q.; Xu, M.; Zhang, J.; Hao, Y.; Qiao, Y.; Zhang, S.; Huang, Q.; Xing, X.; Chen, J. Negative thermal expansion in $(Sc,Ti)Fe_2$ induced by an unconventional magnetovolume effect. *Mater. Horizons* **2019**, *7*, 275−281.

(26) Yang, T.; Lin, K.; Li, Q.; Wang, Y.; Gu, L.; Wang, N.; Deng, J.; Chen, J.; Xing, X. Evidence of the enhanced negative thermal expansion in $(1−x)PbTiO_3$-$xBi(Zn_{2/3}Ta_{1/3})O_3$. *Inorg. Chem. Front.* **2020**, *7*, 1284−1288.

(27) Azuma, M.; Chen, W. T.; Seki, H.; Czapski, M.; Olga, S.; Oka, K.; Mizumaki, M.; Watanuki, T.; Ishimatsu, N.; Kawamura, N.; Ishiwata, S.; Tucker, M. G.; Shimakawa, Y.; Attfield, J. P. Colossal negative thermal expansion in $BiNiO_3$ induced by intermetallic charge transfer. *Nat. Commun.* **2011**, *2*, 347.

(28) Chen, J.; Hu, L.; Deng, J.; Xing, X. Negative thermal expansion in functional materials: controllable thermal expansion by chemical modifications. *Chem. Soc. Rev.* **2015**, *44*, 3522−3567.

(29) Li, Q.; Zhu, H.; Hu, L.; Chen, J.; Xing, X. Negative thermal expansion in nanosolids. *Acc. Chem. Res.* **2019**, *52*, 2694−2702.

(30) Huang, L. F.; Zeng, Z. Roles of mass, structure, and bond strength in the phonon properties and lattice anharmonicity of single-layer Mo and W dichalcogenides. *J. Phys. Chem. C* **2015**, *119*, 18779−18789.

(31) Huang, L. F.; Lu, X. Z.; Rondinelli, J. M. Tunable negative thermal expansion in layered perovskites from quasi-two-dimensional vibrations. *Phys. Rev. Lett.* **2016**, *117*, No. 115901.

(32) Belen'kiĭ, G. L.; Salaev, E. Y.; Suleĭmanov, R. A. Deformation effects in layer crystals. *Sov. Phys. Usp.* **1988**, *155*, 89−127.

(33) Bailey, A. C.; Yates, B. Anisotropic Thermal Expansion of Pyrolytic Graphite at Low Temperatures. *J. Appl. Phys.* **1970**, *41*, 5088−5091.

(34) Belenkii, G. L.; Salaev, E. Y.; Suleimanov, R. A.; Abdullaev, N. A.; Shteinshraiber, V. Y. The nature of negative linear expansion in layer crystals C, BN, GaS, GaSe, and InSe. *Solid State Commun.* **1985**, *53*, 967−971.

(35) Seyidov, M. Y.; Suleymanov, R. A. Negative thermal expansion due to negative area compressibility in $TlGaSe_2$ semiconductor with layered crystalline structure. *J. Appl. Phys.* **2010**, *108*, No. 063540.

(36) Hodgson, S. A.; Adamson, J.; Hunt, S. J.; Cliffe, M. J.; Cairns, A. B.; Thompson, A. L.; Tucker, M. G.; Funnell, N. P.; Goodwin, A. L. Negative area compressibility in silver(I) tricyanomethanide. *Chem. Commun.* **2014**, *50*, 5264−5266.

(37) Jiang, X.; Luo, S.; Kang, L.; Gong, P.; Yao, W.; Huang, H.; Li, W.; Huang, R.; Wang, W.; Li, Y.; Li, X.; Wu, X.; Lu, P.; Li, L.; Chen, C.; Lin, Z. Isotropic negative area compressibility over large pressure range in potassium beryllium fluoroborate and its potential applications in deep ultraviolet region. *Adv. Mater.* **2015**, *27*, 4851−4857.

(38) Liu, X.; George, J.; Maintz, S.; Dronskowski, R. β-CuN_3 :The overlooked ground-state polymorph of copper azide with hetero-graphene-like layers. *Angew. Chem., Int. Ed.* **2015**, *54*, 1954−1959.

(39) Porob, D.; Row, T. N. G. Ab-initio structure determination of $LiBi_3V_2O_{10}$ by powder X-ray diffraction. *Acta Crystallogr. A* **2002**, *58*, 266.

(40) Bruker, AXS *TOPAS V4: General profile and structure analysis software for powder diffraction data-user's Manual*; Bruker, AXS: Karlsruhe, Germany, 2008.

(41) Cliffe, M. J.; Goodwin, A. L. PASCal: a principal axis strain calculator for thermal expansion and compressibility determination. *J. Appl. Crystallogr.* **2012**, *45*, 1321−1329.

(42) Kohn, W.; Sham, L. J. Self-Consistent Equations Including Exchange and Correlation Effects. *Phys. Rev.* **1965**, *140*, A1133.

(43) Clark, S. J.; Segall, M. D.; Pickard, C. J.; Hasnip, P. J.; Probert, M. J.; Refson, K.; Payne, M. C. First principles methods using CASTEP. *Z. Kristallogr.* **2005**, *220*, 567−570.

(44) Perdew, J. P.; Burke, K.; Ernzerhof, M. Generalized gradient approximation made simple. *Phys. Rev. Lett.* **1996**, *77*, 3865−3868.

(45) Perdew, J. P.; Chevary, J. A.; Vosko, S. H.; Jackson, K. A.; Pederson, M. R.; Singh, D. J.; Fiolhais, C. Atoms, molecules, solids, and surfaces: Applications of the generalized gradient approximation for exchange and correlation. *Phys. Rev. B* **1992**, *46*, 6671−6687.

(46) Hamann, D. R.; Schluter, M.; Chiang, C. Norm-conserving pseudopotentials. *Phys. Rev. Lett.* **1979**, *43*, 1494−1497.

(47) Monkhorst, H. J.; Pack, J. D. Special points for brillouin-zone integrations. *Phys. Rev. B* **1976**, *13*, 5188−5192.

(48) Pfrommer, B. G.; Cote, M.; Louie, S. G.; Cohen, M. L. Relaxation of crystals with the quasi-newton method. *J. Comput. Phys.* **1997**, *131*, 233−240.

(49) Baroni, S.; de Gironcoli, S.; Dal Corso, A.; Giannozzi, P. Phonons and related crystal properties from density-functional perturbation theory. *Rev. Mod. Phys.* **2001**, *73*, 515−562.

(50) Adamo, C.; Barone, V. Toward reliable density functional methods without adjustable parameters: The PBE0 model. *J. Chem. Phys.* **1999**, *110*, 6158−6170.

(51) Zachariasen, W. H. The crystal structure of lithium metaborate. *Acta Crystallogr.* **1964**, *17*, 749−751.

(52) Menéndez-Crespo, D.; Costales, A.; Francisco, E.; Martín Pendás, Á. Real-Space In Situ Bond Energies: Toward A Consistent Energetic Definition of Bond Strength. *Chem. − Eur. J.* **2018**, *24*, 9101−9112.

(53) Lu, Z.; Chilukuri, B.; Yang, C.; Rawashdeh, A. M.; Arvapally, R. K.; Tekarli, S. M.; Wang, X.; Cardenas, C. T.; Cundari, T. R.; Omary, M. A. Au$_3$-to-Ag$_3$ coordinate-covalent bonding and other supramolecular interactions with covalent bonding strength. *Chem. Sci.* **2020**, *11*, 11179−11188.

(54) Giddy, A. P.; Dove, M. T.; Pawley, G. S.; Heine, V. The Determination of rigid-unit modes as potential soft modes for displacive phase-transitions in framework crystal-structures. *Acta Crystallogr.* **1993**, *49*, 697−703.

(55) Sasak, T.; Mori, Y.; Yoshimura, M.; Yap, Y. K.; Kamimura, T. Recent development of nonlinear optical borate crystals: key materials for generation of visible and UV light. *Mater. Sci. Eng.* **2000**, *30*, 1−54.